

Perturbative QCD meets phase quenching: The pressure of cold quark matter

Pablo Navarrete,^{1,*} Risto Paatelainen,^{1,†} and Kaapo Seppänen^{1,‡}

¹*Department of Physics and Helsinki Institute of Physics,
P.O. Box 64, FI-00014 University of Helsinki, Finland*

Nonperturbative inequalities constrain the thermodynamic pressure of Quantum Chromodynamics (QCD) with its phase-quenched version, a Sign-Problem-free theory amenable to lattice treatment. In the perturbative regime with a small QCD coupling constant α_s , one of these inequalities manifests as an $O(\alpha_s^3)$ difference between the phase-quenched and QCD pressures at large baryon chemical potential. In this work, we generalize state-of-the-art algorithmic techniques used in collider physics to address large-scale multiloop computations at finite chemical potential, by direct numerical integration of Feynman diagrams in momentum space. Using this novel approach, we evaluate this $O(\alpha_s^3)$ difference and show that it is a gauge-independent and small positive number compared to the known perturbative coefficients at this order. This implies that at high baryon densities, phase-quenched lattice simulations can provide a complementary nonperturbative method for accurately determining the pressure of cold quark matter at $O(\alpha_s^3)$.

I. INTRODUCTION

Determining the bulk thermodynamic properties of strongly interacting matter at the highest temperatures and densities reached in Nature is one of the major challenges in theoretical physics. At high temperatures and small baryon densities, experiments conducted with ultrarelativistic heavy-ion collisions (see e.g. [1] for a review) and theoretical work using nonperturbative lattice simulations [2, 3] have been crucial in understanding the equilibrium properties of Quantum Chromodynamic (QCD) matter. Simultaneously to these developments, the past decade has witnessed rapid progress in the study of neutron stars (NSs). Due to the tight link between NS-matter microphysics and the macroscopic properties of the stars, NSs have become unique cosmic laboratories for studying dense QCD matter (see e.g. [4] for a review). What makes them particularly fascinating in the context of strongly interacting physics is that, unlike any other accessible system in the Universe, the maximal densities reached inside the cores of massive NSs may exceed the limit where nuclear matter undergoes a transition into deconfined cold quark matter (QM) [5, 6].

To describe the thermodynamic properties of dense QCD matter in equilibrium, one needs information about the equation of state (EOS), which relates the pressure p to energy density. Ideally, the EOS should be determined using nonperturbative lattice field theory tools that have provided accurate results in collider environments. Unfortunately, the standard Monte Carlo (MC) techniques fail at finite baryon density due to the Sign Problem [7–13], which prevents lattice QCD simulations in the region of low temperature T and large baryon chemical potential μ_B . Consequently, the only practical methods available to reliably describe the EOS of cold and

dense QCD matter are limited to Chiral Effective Theory, applicable at densities around the nuclear matter saturation density [14–17], and weak-coupling perturbative QCD within high-density QM [18–24]. Several studies [5, 6, 25–30] have shown that systematic interpolations between low- and high-density regions, combined with information from astrophysical NS observations [31–36], can effectively constrain the behavior of the EOS across all densities, provided that accurate asymptotic limits are established at both ends.

Additionally, further bounds for the dense QCD matter EOS can be obtained using phase-quenched (PQ) lattice QCD [37]. In the phase-quenched approximation, the fermion determinant in the QCD partition function for a quark with flavor f , nonzero mass m_f , and chemical potential μ_f is replaced by its magnitude

$$\begin{aligned} \det(\mathcal{D}(\mu_f)) &\rightarrow |\det(\mathcal{D}(\mu_f))| \\ &= \sqrt{\det(\mathcal{D}(\mu_f)) \det(\mathcal{D}(-\mu_f))}, \end{aligned} \quad (1)$$

where the Dirac operator $\mathcal{D}(\mu_f) \equiv \not{D} + m_f + \mu_f \gamma^0$, and the last equality follows from its γ^5 -hermiticity. Here, each phase-quenched fermion corresponds to two copies of “half-species”, appearing in pairs with equal mass but opposite chemical potential. Although this formulation is unphysical, it can constrain the physically more interesting scenarios involving finite μ_B .

For example, consider QCD with two degenerate flavors of light up and down quarks, and a baryon chemical potential $\mu_u = \mu_d = \mu_B/3$. In such a scenario, it follows from Eq. (1) that the phase-quenched partition function is equivalent to the partition function of QCD with a nonzero isospin chemical potential μ_I , where $\mu_u = -\mu_d = \mu_I/2$. Using this observation and nonperturbative QCD inequalities [38], Cohen showed in Ref. [39] that the phase-quenched pressure of isospin matter p_{PQ} serves as a strict upper bound on the QCD pressure of baryonic matter p , i.e. $p_{\text{PQ}}(3\mu_I/2) \geq p(\mu_B)$.

In NS interiors, the energy density may be sufficiently high to give rise to the onset of strange quarks, either

* pablo.navarrete@helsinki.fi

† risto.paatelainen@helsinki.fi

‡ kaapo.seppanen@helsinki.fi

in the form of hyperons or three-flavor QM. Chemical equilibrium under weak interactions (beta-equilibrium) with a nonzero strange quark mass requires $\mu_d = \mu_s$ and $\mu_d > \mu_u$. In this context, Fujimoto and Reddy demonstrated in Ref. [40] that a similar bound to the two-flavor case can be derived for the pressure at nonzero μ_B and μ_I , utilizing additional nonperturbative QCD inequalities derived in Ref. [41]. This inequality necessitates μ_I as a function of μ_B , which remains unknown unless certain model-dependent assumptions are made.

In Ref. [42], Moore and Gorda recently noted that the phase-quenched formulation applies to any arbitrary linear combination of chemical potentials, not limited to μ_I . They suggested that conducting phase-quenched lattice simulations with three-flavor QM could be the most effective method to constrain the NS EOS. Although this phase-quenched configuration of quark chemical potentials represents a completely unphysical system, it holds the potential to provide the most stringent bounds on the physical NS EOS. In particular, at high densities the relative difference between the phase-quenched pressure and the QCD pressure $p_{\text{PQ}} - p$ is perturbatively order α_s^3 in the QCD coupling constant. In any μ -region where this leading $O(\alpha_s^3)$ correction is small, it can be combined with p_{PQ} to provide an improved estimate of p . This estimation would be perturbatively complete up to higher-order corrections in α_s and nonperturbative effects such as pairing gaps [43–46].

In this work, we explicitly evaluate this leading perturbative $O(\alpha_s^3)$ correction. We show that this correction, originating from a single four-loop diagram with two fermion loops connected by three gluons, is a gauge-independent and small positive number compared to the known perturbative coefficients at this order [24]. Hence, phase-quenched lattice simulations can offer a complementary nonperturbative method for accurately determining the pressure of cold and dense quark matter at $O(\alpha_s^3)$. Our diagrammatic evaluation is achieved by generalizing state-of-the-art algorithmic techniques used in collider physics [47–50] to tackle large-scale finite density multiloop integration directly in momentum space. In this approach, one first derives the three-dimensional representation of a Feynman diagram by integrating all the energy components of loop integrals via the residue theorem, followed by the systematic removal of local singularities in the remaining spatial integration space that prevents direct numerical integration, and finally performs the numerical MC evaluation of the remaining finite multi-dimensional spatial momentum integrals. This work represents the first-ever computation of a two-particle-irreducible (2PI) four-loop diagram at finite μ , paving the way toward large-scale automatization of multiloop computations in the context of field theory at finite density.

II. SETUP OF THE CALCULATION

In the context of cold and dense QM with N_f quark flavors, the pressure is given in the grand canonical ensemble by $p = -\Omega$, with Euclidean partition function

$$\mathcal{Z}(\{\mu_j\}) = \int \mathcal{D}A e^{-S[A]} \prod_{j=1}^{N_f} \det(\mathcal{D}(\mu_j)). \quad (2)$$

The perturbative expansion of the pressure then follows as the sum of all connected vacuum Feynman diagrams. The phase-quenched version of this theory makes use of the replacement in Eq. (1), which can be integrated via

$$\sqrt{\det \mathcal{D}(\pm\mu_j)} = \exp \left\{ \frac{1}{2} \text{tr} \log \mathcal{D}(\pm\mu_j) \right\}. \quad (3)$$

The corresponding Feynman rule derived from here amounts to averaging over the sign of each of the quarks' chemical potentials. To see the consequences of this averaging, consider a vacuum-type Feynman diagram $\mathcal{G}(\{\mu_j\})$ in QCD with fermion momenta $P = (p^0 + i\mu_j, \vec{p})$ and bosonic momenta $Q = (q^0, \vec{q})$. Upon the replacement $\mu_j \rightarrow -\mu_j$ for all quarks in \mathcal{G} (i.e. take the complex conjugate), one can make use of the integral's symmetry under flipping the signs of all the fermionic and bosonic loop momenta and the Euclidean QCD Feynman rules to obtain

$$\mathcal{G}(\{-\mu_j\}) = (-1)^{v_q + v_3} \mathcal{G}(\{\mu_j\}) = (-1)^{v - v_4} \mathcal{G}(\{\mu_j\}), \quad (4)$$

with v , v_q , v_3 , and v_4 the number of total, quark-gluon, three-gluon, and four-gluon vertices, respectively. Now, a vacuum-type graph in QCD can only have an odd number of total vertices if it contains an odd number of vertices of valency 4, i.e. four-gluon interactions (see e.g. [51]). Hence, the exponent $v - v_4$ in Eq. (4) is an even number, leading to $\mathcal{G}(\{-\mu_j\}) = \mathcal{G}(\{\mu_j\})$. This implies two things:

1. Vacuum Feynman diagrams are real numbers,
2. Phase-quenched Feynman rules are equivalent to QCD for diagrams with a single quark loop, vanishing in the difference $p_{\text{PQ}}(\{\mu_j\}) - p(\{\mu_j\})$.

Therefore, one expects possible deviations for diagrams containing at least two quark loops.

Let us consider a generic diagram with two quark loops carrying chemical potentials μ_1 and μ_2 , written as

$$\mathcal{G}^\xi(\mu_1, \mu_2) = \int_{Q_b} \mathcal{N}^\xi(Q_b) \Gamma^{(n)}(Q_b, \mu_1) \Gamma^{(m)}(Q_b, \mu_2), \quad (5)$$

where Q_b denotes the set of bosonic loop momenta running through the diagram, and $\mathcal{N}^\xi(Q_b)$ contains all the color traces and the corresponding bosonic Feynman rules, for general covariant gauges parametrized by ξ ; $\Gamma^{(n)}$ is an insertion of a gluon n -point function with one quark loop (suppressing Lorentz indices and stripping off

color factors). By averaging over the sign of the chemical potentials, we can compute the contribution of \mathcal{G} to $p_{\text{PQ}}(\mu_1, \mu_2) - p(\mu_1, \mu_2)$ keeping in mind that vacuum diagrams are real, reducing the number of independent terms from four to only two. As reversing the sign of μ in a quark-loop insertion in Eq. (5) is equivalent to complex conjugation, we get altogether

$$\begin{aligned} p_{\text{PQ}} - p \Big|_{\mathcal{G}} &= -\frac{1}{2} [\mathcal{G}^\xi(\mu_1, \mu_2) - \mathcal{G}^\xi(\mu_1, -\mu_2)] \\ &= \int_{Q_b} \mathcal{N}^\xi(Q_b) \text{Im} \Gamma^{(n)}(Q_b, \mu_1) \text{Im} \Gamma^{(m)}(Q_b, \mu_2). \end{aligned} \quad (6)$$

Here, we made use of the fact that bosons do not carry chemical potentials, implying \mathcal{N} is real and therefore only the imaginary parts of the quark-loop insertions give non-zero contributions to $p_{\text{PQ}} - p$.

The various cancellations occurring in Eq. (6) can be represented pictorially as

$$\begin{aligned} p_{\text{PQ}} - p \Big|_{\mathcal{G}} &= \left(\text{Diagram 1} \right)_{\text{PQ}} - \left(\text{Diagram 2} \right)_{\text{PQ}} + i \times (\text{cross terms}) - \left(\text{Diagram 3} \right)_{\text{full QCD}} \\ &= \left(\text{Diagram 4} \right)_{\text{Im}}, \end{aligned} \quad (7)$$

where the cross terms of real and imaginary parts vanish as a consequence of vacuum diagrams being real quantities, while the effect of the subtracted phase-quenched diagram is understood as setting the contribution of the fully real combination of quark-loop insertions in full QCD to zero. Consequently, one should search for the simplest insertions of quark loops that involve non-zero imaginary parts. One can readily see that the one-loop gluon two-point function, defined as

$$\Gamma_{\alpha\beta}^{(2)}(Q, \mu_j) = \int_{\{P\}_j} \frac{\text{tr} [\not{P} \gamma_\alpha (\not{P} - \not{Q}) \gamma_\beta]}{P^2(P-Q)^2}, \quad (8)$$

is a real function, as complex conjugation is equivalent to

the shift $P \rightarrow Q - P$, which is a symmetry of the integral. Here, $\int_{\{P\}_j} f(P^0, \vec{p}) \equiv \int \frac{d^4 p}{2\pi} \int \frac{d^3 \vec{p}}{(2\pi)^3} f(p^0 + i\mu_j, \vec{p})$ denotes the 4-dimensional fermionic loop momentum integral.

It turns out that this argument no longer applies to the one-loop three-point function, as this integral has no symmetries of this type. One then expects that the leading order contribution to $p_{\text{PQ}} - p$ is a diagram composed of two quark loops connected by three gluon lines, entering at four loops: “the Bugblatter” [52]. In fact, there are two diagrams of this type with differing relative fermion flows, and their explicit expressions using the QCD Feynman rules, up to the terms proportional to ξ , are as follows:

$$\begin{aligned} \text{Diagram A} &= \frac{g_s^6}{6} \mathcal{T}^{abc} \mathcal{T}^{abc} \sum_{i,j=1}^{N_f} \left\{ \int_{Q\{P\}_i\{R\}_j^* S} \frac{-\text{tr} [\not{P} \gamma^\mu (\not{P} - \not{S}) \gamma^\nu (\not{Q} - \not{P}) \gamma^\sigma] \text{tr} [\not{R} \gamma^\mu (\not{R} - \not{S}) \gamma^\nu (\not{Q} - \not{R}) \gamma^\sigma]}{Q^2 P^2 R^2 S^2 (P-S)^2 (R-S)^2 (Q-P)^2 (Q-R)^2 (Q-S)^2} \right\}, \\ \text{Diagram B} &= \frac{g_s^6}{6} \mathcal{T}^{cba} \mathcal{T}^{abc} \sum_{i,j=1}^{N_f} \left\{ \int_{Q\{P\}_i\{R\}_j S} \frac{+\text{tr} [\not{P} \gamma^\mu (\not{P} - \not{S}) \gamma^\nu (\not{Q} - \not{P}) \gamma^\sigma] \text{tr} [\not{R} \gamma^\sigma (\not{Q} - \not{R}) \gamma^\nu (\not{R} - \not{S}) \gamma^\mu]}{Q^2 P^2 R^2 S^2 (P-S)^2 (R-S)^2 (Q-P)^2 (Q-R)^2 (Q-S)^2} \right\}. \end{aligned} \quad (9)$$

Here, $g_s = \sqrt{4\pi\alpha_s}$, and we have made use of the shorthand notation $\mathcal{T}^{abc} \equiv \text{tr}(T^a T^b T^c)$ for the color trace in quark loops. Note the \mathcal{T}^{cba} factor in the second line of Eq. (9), coming from the relative flow orientation of the N_f quark flavors running in the loops, which we sum

over.

Denoting the integral expressions inside the curly brackets for each diagram by $B_1^\xi(\mu_i, \mu_j)$ and $B_2^\xi(\mu_i, \mu_j)$, respectively, the Dirac traces can be related through

charge conjugation, giving

$$B_2^\xi(\mu_i, \mu_j) = -B_1^\xi(\mu_i, -\mu_j). \quad (10)$$

This is just a manifestation of Furry's theorem, as pointed out in Ref. [42]. On the other hand, in terms of the $SU(N_c)$ structure constants f^{abc} and the totally symmetric group invariant d^{abc} , the color traces entering Eq. (9) read

$$\mathcal{T}^{abc} = \frac{1}{4}(d^{abc} + if^{abc}) = (\mathcal{T}^{cba})^*, \quad (11)$$

implying that the Bugblatter diagrams contain the two color structures $d^{abc}d^{abc}$ and $f^{abc}f^{abc}$. Crucially, the complex conjugation property in Eq. (11) results in a relative sign in the $f^{abc}f^{abc}$ pieces.

With these relations at hand, we proceed to construct $p_{\text{PQ}} - p$ as shown above, by averaging over the N_f chemical potentials running in the loops, for both diagrams. As instructed in the NS setup, we specialize to the case of asymptotically dense three-flavor ($N_f = 3$) unpaired QM in beta-equilibrium, where quarks can be considered massless and quark chemical potentials are equal. We set $\mu_i = \mu_B/3$ for all quarks, obtaining altogether

$$p_{\text{PQ}}(\mu_B) - p(\mu_B) = \frac{-3^2}{6 \times 3^4} \frac{d^{abc}d^{abc}}{16} g_s^6 \times \left[B_1^\xi(\mu_B, \mu_B) - B_1^\xi(\mu_B, -\mu_B) \right] + O(g_s^8), \quad (12)$$

where an additional factor of 3^4 appears through the scaling of B_1^ξ upon replacing μ_i^4 by μ_B^4 . Note that the $f^{abc}f^{abc}$ part cancels in the difference $p_{\text{PQ}} - p$, and therefore only $d^{abc}d^{abc} = (N_c^2 - 1)(N_c^2 - 4)/N_c$ survives. Notably, the resulting combination of diagrams entering Eq. (12) is precisely of the form found in the Bugblatter contribution to QED, with the vanishing $f^{abc}f^{abc}$ piece being of purely non-Abelian nature. As a result, the expression in Eq. (12) satisfies several properties, as we demonstrate in the following.

Firstly, expanding the diagrams in general covariant gauge in terms of scalarized integrals, one obtains a quadratic polynomial in the gauge parameter ξ . At this point, one can already appreciate the complexity of these diagrams, as they contain all nine non-factorized planar QCD vacuum topologies at four loops [53]. Upon exploiting linear relations among these integrals, in the form of momentum shifts stemming from the graphs' internal symmetries [54, 55], we explicitly checked that the gauge parameter cancels out at the integrand level in the sum entering Eq. (12), rendering this combination gauge invariant. Consequently, in the following, we set $\xi = 0$ and drop the superscript ξ .

Secondly, we can prove that this expression is automatically positive, as expected from the nonperturbative inequality $p_{\text{PQ}} \geq p$. In effect, the prefactor in Eq. (12) is nonpositive for all N_c , so it suffices to show that the difference inside the square brackets is negative, a combination being precisely of the form encountered in Eq. (6).

As bosonic propagators are real and positive in the whole region of integration, one has

$$B_1(\mu_B, \mu_B) - B_1(\mu_B, -\mu_B) = -2 \int_{QS} \frac{[\text{Im} \Gamma_{\mu\nu\sigma}^{(3)}(Q, S, \mu_B)]^2}{Q^2 S^2 (Q - S)^2} \leq 0, \quad (13)$$

proving that the leading-order contribution to $p_{\text{PQ}} - p$ is positive.

Thirdly, we can argue that it is infrared (IR) finite. Indeed, the infrared physics of these diagrams is properly captured by the hard-thermal-loop (HTL) limit of the three-gluon vertex function, whose color structure is $\Gamma_{\text{HTL}}^{(3)} \sim f^{abc}$ [22]. This means that only the $f^{abc}f^{abc}$ piece of the Bugblatter diagrams, canceling in the difference $p_{\text{PQ}} - p$, develops a logarithmic infrared divergence. Consequently, the structure $d^{abc}d^{abc}$ in Eq. (12) which we compute here must be infrared finite (see also [42]), further implying that non-analytic logarithms in the coupling arising from the HTL resummation do not appear at this order, but can potentially enter only at order $O(\alpha_s^4 \ln^n \alpha_s)$.

Finally, we argue that Eq. (13) is ultraviolet (UV) finite. One might expect this based on the observation that there are no lower loop diagrams with the color factor $d^{abc}d^{abc}$ that could renormalize Eq. (12). Indeed, this combination picks up the imaginary part of the vertex function, a quantity that vanishes in the ultraviolet due to this limit being pure vacuum (i.e. $i\mu \rightarrow 0$). Thus, only the $f^{abc}f^{abc}$ piece of the Bugblatter diagrams entering full QCD, containing the real part of the vertex function, requires renormalization.

III. A NEW NUMERICAL APPROACH

To proceed with the evaluation of the fully finite four-loop momentum integrals displayed in Eq. (13), we next introduce a novel approach to numerical multiloop integration at finite density.

In modern quantum field theory, multiloop Feynman diagrams are often first expanded in terms of scalarized integrals, which are then systematically reduced to a basis of so-called master integrals through large-scale automated algorithmic procedures based on solving integration-by-parts (IBP) identities [56, 57]. In this context, techniques for computing master integrals in dimensional regularization are highly developed [58]. However, in a thermal setup (finite μ and/or T) we break Lorentz symmetry, limiting the usage of the traditional techniques that have proven successful in the vacuum setting. Despite this, all thermal cases relevant to the pressure up to the three-loop level have been managed on a case-by-case basis [59, 60]. This is achieved through brute-force semi-analytical calculation of the scalarized integrals, which rely on tedious subtractions of divergences at the level of one-loop self-energy insertions. At

the four-loop level, the presence of integral topologies containing more complicated substructures severely restricts the implementation of this method to only the simplest cases [61–63], calling for the development of new tools and methods to handle multiloop calculations beyond three loops.

At finite density, proposed approaches in this direction include the so-called cutting rules method, which was introduced in Refs. [18, 64], and a generalization of IBP to finite density, developed in Ref. [65]. While the latter has not yet been explored even at three loops, the former has been successfully employed at this level in Ref. [18]. In the cutting rules, a representation of Feynman integrals is derived by integrating the energy components of fermionic loops via the residue theorem, resulting in a sum of three-dimensional phase-space integrals over on-shell amplitudes at zero μ . However, a generic obstacle in this approach is that the dimensionally regulated phase-space integrals introduce spurious IR divergences not present in the original Feynman integral, complicating their calculation even for the simplest four-loop topologies.

Recent developments in high-performance numerical evaluation of Feynman diagrams directly in momentum space, such as the Loop-Tree Duality (LTD) (see e.g. [47, 48]), offer a promising alternative avenue to multiloop integration. The defining feature these techniques capitalize on is the analytical computation of both fermionic and bosonic energy integrals via the residue theorem, in contrast to the cutting rules method. This approach is particularly suitable for finite-density calculations due to the effect of the chemical potentials being entirely encoded in the temporal momentum components.

Inspired by the LTD and related ideas, we put forward a novel generalization of these approaches to finite-density field theory, which we call dense LTD (dLTD). Specifically, we implement numerical MC integration routines for the spatial momentum integrals, preceded by an analytical computation of zero-component (energy) residues. This is realized by restructuring the integrand into a convenient representation, allowing for the systematic removal of local spurious (integrable) singularities that hinder direct numerical integration.

A. Derivation of dLTD

In the following, we provide a finite- μ generalization of the algorithm introduced in Ref. [50] for computing the energy integrals, employing the notation introduced therein. Let $\mathbf{x} = (x_i)_{i \in \{1, \dots, n\}}$ denote a vector with n components, $\mathbf{x} \cdot \mathbf{y} = \sum_{i=1}^n x_i y_i$ the standard scalar product of two vectors \mathbf{x} and \mathbf{y} , and $\mathbf{x} \odot \mathbf{y} = (x_i y_i)_{i \in \{1, \dots, n\}}$ component-wise multiplication of the vectors. Now, a vacuum-type l -loop integral with n single-power propagators at finite μ , stripped of its spatial loop integrations

over \vec{p}_i , can be written as

$$I \equiv \int \left[\prod_{i=1}^l \frac{dp_i^0}{2\pi} \right] \frac{\mathcal{N}(\mathbf{Q}^0)}{\prod_{j=1}^n \left[(Q_j^0)^2 + E_j^2 \right]}, \quad (14)$$

where the numerator \mathcal{N} is a regular function of the propagator energies $\mathbf{Q}^0 = \sum_{i=1}^l \mathbf{S}_i p_i^0 + i\boldsymbol{\varphi}\mu$, the vectors $\mathbf{S}_i = (S_{1i}, \dots, S_{ni})$ with $S_{ji} \in \{\pm 1, 0\}$ fix the loop momentum basis, and the vector $\boldsymbol{\varphi} = \sum_{i=1}^l \mathbf{S}_i \tilde{\varphi}_i \in \{\pm 1, 0\}^n$ with $\tilde{\varphi}_i \in \mathbb{Z}$ determines the fermion signature of each propagator. The propagator on-shell energies are given by $E_j^2 = |\vec{q}_j|^2 + m_j^2$, where the spatial loop momenta are $\vec{\mathbf{q}} = \sum_{i=1}^l \mathbf{S}_i \vec{p}_i$ and the masses are denoted by m_j .

We start the derivation by inserting the unity

$$1 = \int d\tilde{p}_j^0 \delta \left(\tilde{p}_j^0 - \sum_{i=1}^l S_{ji} p_i^0 \right) \quad (15)$$

for each propagator in Eq. (14) and writing the Dirac deltas as integrals over the variables τ_j ,

$$I = \int \prod_{i=1}^l \frac{dp_i^0}{2\pi} \int \prod_{j=1}^n d\tau_j e^{-i\tau_j \sum_{i=1}^l S_{ji} p_i^0} \times \int \left[\prod_{j=1}^n \frac{d\tilde{p}_j^0}{2\pi} \frac{e^{i\tau_j \tilde{p}_j^0}}{(\tilde{p}_j^0 + i\varphi_j \mu)^2 + E_j^2} \right] \mathcal{N}(\tilde{\mathbf{p}}^0 + i\boldsymbol{\varphi}\mu). \quad (16)$$

Now the energy integrals over \tilde{p}_i^0 can be performed for each propagator independently. Using residue calculus, we obtain

$$I = \int \prod_{i=1}^l \frac{dp_i^0}{2\pi} \int \prod_{j=1}^n d\tau_j e^{-i\tau_j \sum_{i=1}^l S_{ji} p_i^0} \times \left[\prod_{j=1}^n \frac{1}{2E_j} \sum_{\rho_j, \sigma_j \in \{\pm 1\}} \rho_j \sigma_j e^{-\tau_j (\rho_j E_j - \varphi_j \mu)} \right] \times \Theta(\sigma_j (\rho_j E_j - \varphi_j \mu)) \Theta(\sigma_j \tau_j) \mathcal{N}(i\boldsymbol{\rho} \odot \mathbf{E}). \quad (17)$$

Changing the integration variables as $\boldsymbol{\tau} \rightarrow \boldsymbol{\sigma} \odot \boldsymbol{\tau}$, renaming $\boldsymbol{\rho} \odot \boldsymbol{\sigma} \rightarrow \boldsymbol{\rho}$, $\boldsymbol{\sigma} \rightarrow \boldsymbol{\sigma}$, writing the integrals over p_i^0 as Dirac delta functions, and reorganizing yields

$$I = \sum_{\substack{\boldsymbol{\rho} \in \{\pm 1\}^n \\ \boldsymbol{\sigma} \in \{\pm 1\}^n}} \mathcal{N}(i\boldsymbol{\sigma} \odot \boldsymbol{\rho} \odot \mathbf{E}) \prod_{j=1}^n \frac{\Theta(\rho_j E_j - \sigma_j \varphi_j \mu)}{2\rho_j E_j} \times \int_{\mathbb{R}_+^n} d\boldsymbol{\tau} e^{-\boldsymbol{\tau} \cdot (\boldsymbol{\rho} \odot \mathbf{E})} \prod_{i=1}^l \delta(\boldsymbol{\tau} \cdot (\boldsymbol{\sigma} \odot \mathbf{S}_i)), \quad (18)$$

where the exponential has simplified due to the property $\boldsymbol{\tau} \cdot (\boldsymbol{\sigma} \odot \boldsymbol{\varphi}) = \sum_{i=1}^l \tilde{\varphi}_i \boldsymbol{\tau} \cdot (\boldsymbol{\sigma} \odot \mathbf{S}_i)$. Before this simplification, the expression in the parenthesis in the exponent matches the arguments of the step functions.

In contrast to the vacuum case presented in Ref. [50], the generalization in Eq. (18) involves step functions that include μ , along with an additional sum over the sign vectors ρ . However, the integral on the second line of Eq. (18), representing a Laplace transform of a non-simplicial convex cone, is an object already encountered in the vacuum computation. We perform this integral using the algorithmic procedure described in Ref. [50], leading to a sum of rational functions of linear combinations of the on-shell energies E_i . The resulting representation for the spatial integral is free of spurious divergences, making it particularly suitable for direct numerical integration.

Nonetheless, the expression resulting from Eq. (18) often contains integrable singularities that can impair the accuracy of MC integration. To address this issue, we have implemented a multichanneling technique similar to the one presented in Ref. [49], as detailed in Appendix A. This procedure decomposes the integrand into a sum of multiple terms (channels), with each channel parametrized in such a way that its Jacobian flattens integrable singularities specific to that channel.

B. Cross-checks of dLTD

To verify the validity of our numerical approach, we have cross-checked that our dLTD implementation in Eq. (18) reproduces several analytically known cases in both vacuum and finite-density field theory. As a baseline check, we first compute a nontrivial UV- and IR-finite, fully massive four-loop Bugblatter-type diagram with a trivial numerator at zero density. The comparison between our numerical result using the zero-density limit of dLTD and the analytical result from Ref. [66] is displayed in the first row of Table I. Using the VEGAS5.6 integration routine [67] with approximately 10^9 MC samples, we obtained $2.16931(4) \cdot 10^{-9}$, which matches the analytical result $2.16928 \cdot 10^{-9}$ to the first five digits. For the finite density case, we perform comparisons between our dLTD results and analytical calculations for UV-subtracted, IR-finite, two- and three-loop vacuum-type QCD diagrams with massless quarks [59]. Details for these cases can be found in Appendix C. The results are shown in the last two rows of Table I, where we observe an excellent agreement including the first four digits. In the last column of the table, we present the timing per sample per core for our computation, demonstrating efficient scaling on the number of loops.

IV. RESULTS AND DISCUSSION

We are now prepared to evaluate the new coefficient in Eq. (13) using the integrand representation generated by Eq. (18). With a suitable choice of coordinates (see Appendix B), this leads to a nine-dimensional integral over the spatial momenta. We compute this integral nu-




Diagram	Analytic	dLTD	$N [10^6]$	$[\mu\text{s}]$
	$2.16928 \cdot 10^{-9}$ [66]	$2.16931(4) \cdot 10^{-9}$	3000	5.2
	-0.00128325 [59]	$-0.00128338(23)$	150	5.8
	-0.000256547 [59]	$-0.00025654(9)$	800	9.6

TABLE I. Numerical integration via our approach compared against analytic results from Refs. [59, 66] for IR- and UV-finite massive four-loop scalar diagram at $\mu = 0$ and IR-finite two- and three-loop QCD diagrams at finite μ (here set to 1). The UV divergence of the three-loop diagram has been subtracted away in the $\overline{\text{MS}}$ scheme, while $g_s = N_f = 1$, $N_c = 3$, and $\Lambda = \mu$. N denotes the MC statistics and $[\mu\text{s}]$ is the timing per sample per core in microseconds.

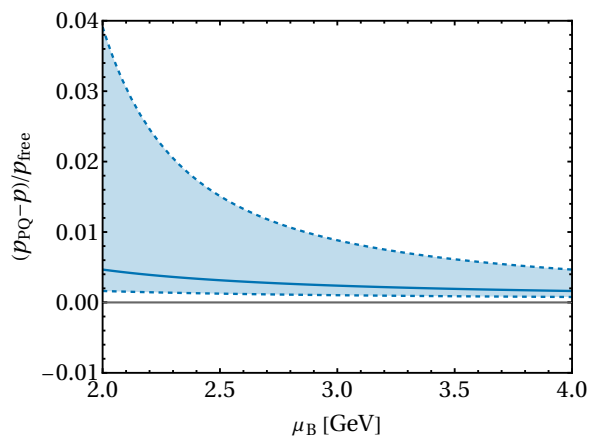


FIG. 1. The leading-order difference between the pressure of three-flavor dense QM and its phase-quenched version, normalized by the free pressure, as a function of the baryon chemical potential. The shaded region shows the scale variation of $X \in [1/2, 2]$, while the solid curve is the central value $X = 1$.

merically employing the VEGAS5.6 integration routine [67], distributing roughly $6 \cdot 10^{11}$ MC samples across 75 channels (see Appendix A) and spending 7 microseconds per sample per core on average. We determine the new coefficient as

$$B_1(\mu_B, \mu_B) - B_1(\mu_B, -\mu_B) = -3.327(7) \cdot 10^{-6} \mu_B^4, \quad (19)$$

where the MC error in the numerical result is negligible for practical purposes. Additionally, the cancellation of IR divergences in Eq. (13) is non-local, necessitating a regularization procedure for numerical evaluation. To address this, we introduce a small but nonzero mass in the gluon propagators, which effectively screens these residual IR singularities. Since the integrated result is IR finite, as discussed in Section II, it should remain insensitive to the small value of the regulator. We have verified this insensitivity by varying the gluon mass within the range $[10^{-5} \mu_B, 10^{-2} \mu_B]$ (see Appendix D).

By utilizing Eq. (12) and setting $N_c = 3$, we then find

that the relative difference $p_{\text{PQ}} - p$ in the perturbative region is

$$p_{\text{PQ}}(\mu_{\text{B}}) - p(\mu_{\text{B}}) = 3.368(7) \cdot \left(\frac{\alpha_s(\bar{\Lambda})}{\pi} \right)^3 p_{\text{free}}, \quad (20)$$

where $\alpha_s = \alpha_s(\bar{\Lambda})$ represents the renormalized strong coupling constant in the $\overline{\text{MS}}$ scheme at the renormalization scale $\bar{\Lambda}$, and we have written our result in terms of the pressure of a free Fermi gas of quarks in beta equilibrium, denoted as $p_{\text{free}} = 3(\mu_{\text{B}}/3)^4/4\pi^2$.

In Fig. 1, we display the relative difference $p_{\text{PQ}} - p$ normalized by the free quark pressure as a function of μ_{B} . We employ the known three-loop running for $\alpha_s(\bar{\Lambda})$, set $\bar{\Lambda} = 2X\mu_{\text{B}}/3$, and estimate the uncertainty arising from truncating the perturbative series by varying X in the range $[1/2, 2]$. It is observed that in the perturbative region $\mu_{\text{B}} \gtrsim 2.5$ GeV, corresponding to $\alpha_s \lesssim 0.5$, the difference $p_{\text{PQ}} - p$ is very small. This implies that phase-quenched lattice simulations provide an accurate approximation for the dense QM pressure in the perturbative regime.

A few comments on the significance of our results are in order. First, we have generalized state-of-the-art algorithmic techniques used in collider physics to handle large-scale multiloop computations at finite chemical potential, by direct numerical integration of Feynman diagrams in momentum space. This novel technique allowed us to perform the first-ever finite- μ computation of a 2PI four-loop diagram, being part of the most complicated vacuum topology in QCD. We stress that our new approach, which we call dLTD, is not limited to the calculation presented in this work, but it is equally applicable to diagrams of various topologies at the four-loop level, in addition to holding the prospect of being generalizable to the case of diagrams with external legs. Second, our numerical evaluation of the leading $O(\alpha_s^3)$ perturbative correction to the difference $p_{\text{PQ}}(\mu_{\text{B}}) - p(\mu_{\text{B}})$ demonstrates that Sign-Problem-free lattice simulations can provide a complementary method for accurately evaluating the pressure of cold and dense QM at $O(\alpha_s^3)$. Finally, we present an estimate for the necessary accuracy of phase-quenched lattice simulations to effectively constrain the EOS of QM at high density. Drawing upon the latest state-of-the-art perturbative findings (see the right panel in Fig. 2 of Ref. [24]), we approximate that the uncertainty in phase-quenched lattice simulations should be less than 25% for $\mu_{\text{B}} \geq 2.2$ GeV.

As a closing remark, we believe the results presented in this paper will play a significant role in achieving the goal of determining the $O(\alpha_s^3)$ EOS of dense quark matter. We emphasize that this could have a major impact on the inference of the neutron star matter EOS, potentially leading to a true breakthrough in understanding the properties of matter in neutron-star cores.

ACKNOWLEDGMENTS

We thank Zeno Capatti, Valentin Hirschi, Aleksi Kurkela, Heikki Mäntysaari, York Schröder, Saga Säppi, and Aleksi Vuorinen for their helpful comments and suggestions. P.N., R.P., and K.S. have been supported by the Academy of Finland grants no. 347499 and 353772. P.N. is also supported by the Doctoral School of the University of Helsinki, and K.S. is additionally supported by the Finnish Cultural Foundation. We also wish to acknowledge CSC – IT Center for Science, Finland, for computational resources. Feynman diagrams were drawn using Axodraw [68].

Appendix A: Multichanneling at finite density

Loop momentum integrals, after integrating over the temporal direction (see e.g. Eq. (C6)), often exhibit sharp enhancements, which become integrable singularities in the case of massless propagators. These singularities can significantly hinder numerical integration. However, by employing a technique called multichanneling, it is possible to systematically remove these enhancements, provided their location and approximate functional form are known. We have implemented the multichanneling method, based on the approach described in Ref. [49], and modified it to accommodate the singularity structure specific to finite- μ loop integrals.

At vanishing μ , the general functional form of the enhancements is given by [49]:

$$\sum_{b \in \mathcal{B}} \prod_{i \in b} E_i^{-1}, \quad (A1)$$

where \mathcal{B} denotes the set of all loop momentum bases, and E_i is the on-shell energy of propagator i . At finite μ , the form of the bosonic enhancements remains unchanged, as bosons do not carry μ . However, fermionic enhancements at $E_i = 0$ cancel when $\mu > 0$. This is evident from Eq. (18); in the limit where a fermionic on-shell energy vanishes, the E_i^{-1} enhancement cancels in the sum over ρ . Instead, fermionic singularities can occur at the intersections of Fermi surfaces, $E_i = E_j = \mu$, where the argument of the exponent in Eq. (18) can vanish. After performing the τ integral, these integrable singularities take the form

$$\frac{\Theta(E_i - \mu)\Theta(\mu - E_j)}{E_i - E_j}, \quad (A2)$$

where the on-shell energies E_i and E_j approach μ from different directions. Therefore, a functional form that captures both the bosonic and at least part of the fermionic enhancements at finite μ is

$$\sum_{b \in \mathcal{B}} \prod_{i \in b} |E_i - |\varphi_i|\mu|^{-1}, \quad (A3)$$

where φ_i is the fermion signature of propagator i .

Let \mathcal{I} be an integrand of a spatial loop integral. To flatten the above enhancements in \mathcal{I} , we divide and multiply \mathcal{I} by Eq. (A3) and then split up the sum over \mathcal{B} in the numerator into $|\mathcal{B}|$ channels,

$$\mathcal{I} = \sum_{b \in \mathcal{B}} \mathcal{C}_b, \quad \mathcal{C}_b \equiv \frac{\mathcal{I}}{\underbrace{\sum_{c \in \mathcal{B}} \prod_{j \in c} |E_j - |\varphi_j| \mu|^{-1}}_{\text{enhancements cancel}}} \prod_{i \in b} |E_i - |\varphi_i| \mu|^{-1}. \quad (\text{A4})$$

The enhancements canceled by the factor in Eq. (A3) are now split into different channels specified by the loop momentum bases b . To remove these enhancements, we parameterize each channel \mathcal{C}_b differently. We choose the loop momentum variables to be the momenta of the propagators in b , $\{\vec{p}_i\}_{i \in b}$, so that the Jacobian introduced in Appendix B flattens the peak structure $\prod_{i \in b} |E_i - |\varphi_i| \mu|^{-1}$.

Appendix B: Parametrization for the spatial integrals

The Monte-Carlo integrator VEGAS5.6 [67] is employed to compute the spatial integrals over \mathbb{R}^{3l} , where l represents the number of loops. This integrator generates points within the unit hypercube $[0, 1]^{3l}$. To create sample configurations for the spatial loop momenta, these points are then transformed to \mathbb{R}^{3l} using a Cartesian product of spherical parametrizations [49]. Specifically, for each loop momentum $\vec{p} = (p_x, p_y, p_z)$, a point in the 3D unit cube, $(x_1, x_2, x_3) \in [0, 1]^3$, is mapped to $(p_x, p_y, p_z) \in \mathbb{R}^3$ using the transformation

$$\begin{aligned} p_x &= r \sin \theta \cos \phi, & r &= h_a(x_1), \\ p_y &= r \sin \theta \sin \phi, & \theta &= \arccos(-1 + 2x_2), \\ p_z &= r \cos \theta, & \phi &= 2\pi x_3, \end{aligned} \quad (\text{B1})$$

with

$$h_a(x) = \begin{cases} p_F - \left| \frac{\mu^a x}{1-x} - p_F^a \right|^{1/a}, & x < \frac{p_F^a}{\mu^a + p_F^a} \\ p_F + \left| \frac{\mu^a x}{1-x} - p_F^a \right|^{1/a}, & x \geq \frac{p_F^a}{\mu^a + p_F^a} \end{cases}, \quad (\text{B2})$$

and the Jacobian

$$J = \frac{4\pi}{a\mu^a} r^2 |r - p_F|^{1-a} (\text{sgn}(r - p_F) |r - p_F|^a + p_F^a + \mu^a)^2. \quad (\text{B3})$$

For fermionic loop momenta \vec{q} , $p_F = \sqrt{\mu^2 - m^2}$ when $\mu > m$; otherwise, $p_F = 0$. Here, μ and m represent the

chemical potential and mass as they appear in the propagator associated with \vec{q} . Additionally, the parameter a must satisfy $a > 0$. This specific parametrization is chosen because its Jacobian vanishes at the Fermi surface when $a < 1$, thereby flattening integrable singularities at the surface (see Appendix A). In this work, we have set $a = 1/2$.

The above parametrization is general and does not consider any symmetries that the integrand might have. However, in our case, the integrands enjoy rotational symmetry since the vacuum-type diagrams are independent of any external momenta. By exploiting this symmetry, we reduce the dimensionality of the numerical spatial integral from $3l$ to $3l - 3$ (or 1 for $l = 1$). This reduction is achieved by fixing the polar and azimuthal angles of the first loop momentum such that $\vec{p}_1 = (0, 0, r_1)$, and fixing the azimuthal angle of the second loop momentum such that $\vec{p}_2 = (r_2 \sin \theta_2, 0, r_2 \cos \theta_2)$. This allows for the analytical integration of these trivial angular integrals. The remaining loop momenta are then parametrized with their full angular dependence according to Eq. (B1).

Appendix C: Two-loop example for dLTD

Here, we outline some details of the semi-numerical algorithm we use for computing multiloop integrals at finite chemical potential μ . The example we consider is the two-loop sunset diagram, which is also presented in Table I. It reads

$$\text{Sunset Diagram} = -\frac{g_s^2}{2} N_f \text{tr} [T^a T^a] \int_{\{P_1, P_2\}} \frac{\text{tr} [\not{P}_1 \gamma^\mu \not{P}_2 \gamma_\mu]}{P_1^2 P_2^2 (P_1 - P_2)^2}, \quad (\text{C1})$$

where $\int_{\mathcal{P}} \equiv \int d^4 P / (2\pi)^4$, and the curly brackets in the integration measure denote fermionic momenta, for which the energy components are shifted by $+i\mu$.

Unlike the UV- and IR-finite combination of the Bugblatter diagrams, the two-loop sunset diagram is superficially UV-divergent. These divergences must be subtracted locally at the integrand level for numerical integration. To achieve this, we employ Bogoliubov's recursive R -operation [69–71], which subtracts several counterterms from a given Feynman diagram to capture all (possibly nested) UV divergences. Within the R -operation, we implement local UV renormalization operators K , as constructed in Ref. [72], rendering the given integral UV-finite at the integrand level. In practice, applying the R -operation to the sunset diagram yields (for details, see Ref. [72])

$$\begin{aligned}
R \left(\text{Sunset Diagram} \right) &= \text{Sunset Diagram} - \text{Bubble Diagram} * K \left(\text{Wavy Sunset Diagram} \right) - \text{Bubble Diagram} * K \left(\text{Wavy Sunset Diagram} \right) - \text{Wavy Bubble Diagram} * K \left(\text{Wavy Sunset Diagram} \right) \\
&- K \left(\text{Sunset Diagram} \right) + K \left(\text{Bubble Diagram} * K \left(\text{Wavy Sunset Diagram} \right) \right) + K \left(\text{Bubble Diagram} * K \left(\text{Wavy Sunset Diagram} \right) \right) \\
&+ K \left(\text{Wavy Bubble Diagram} * K \left(\text{Wavy Sunset Diagram} \right) \right),
\end{aligned} \tag{C2}$$

where $*$ denotes the contraction of tensor indices, and K is an operator that extracts the UV divergences of the graph it acts on. Specifically, $K(\gamma)$ Taylor expands the integrand corresponding to a graph γ in the limit where the loop momenta of γ go to infinity, up to the order specified by the superficial degree of divergence (dod) of γ . Additionally, since thermal effects vanish exponentially

in the UV, K sets the chemical potential μ appearing in γ to zero. Consequently, $K(\gamma)$ is a sum of single-scale tensor integrals, where the numerators depend polynomially on the external momenta and masses of γ , and all the propagators have the same mass m_{UV} that is introduced for ensuring the IR-finiteness of the counterterms. As an illustrative example, let us consider one of the K -operations appearing in Eq. (C2) explicitly as

$$\begin{aligned}
K \left(\text{Wavy Sunset Diagram} \right) &= K \left(-g_s^2 T^a T^a \int_{\{P_2\}} \frac{\gamma^\mu \not{P}_2 \gamma_\mu}{P_2^2 (P_1 - P_2)^2} \right) \\
&= -g_s^2 T^a T^a \left\{ \int_{P_2} \frac{\gamma^\mu \not{P}_2 \gamma_\mu}{(P_2^2 + m_{\text{UV}}^2)^2} + \int_{P_2} \frac{2P_1 \cdot P_2 \gamma^\mu \not{P}_2 \gamma_\mu}{(P_2^2 + m_{\text{UV}}^2)^3} \right\},
\end{aligned} \tag{C3}$$

where the expansion is carried out to the next-to-leading order dictated by the graph's superficial dod of one. The

expanded tensor integral in Eq. (C3) is then contracted with the remaining graph, resulting in

$$\text{Bubble Diagram} * K \left(\text{Wavy Sunset Diagram} \right) = -\frac{g_s^2}{2} N_f \text{tr} [T^a T^a] \left\{ \int_{\{P_1\}P_2} \frac{\text{tr} [\not{P}_1 \gamma^\mu \not{P}_2 \gamma_\mu]}{P_1^2 (P_2^2 + m_{\text{UV}}^2)^2} + \int_{\{P_1\}P_2} \frac{2P_1 \cdot P_2 \text{tr} [\not{P}_1 \gamma^\mu \not{P}_2 \gamma_\mu]}{P_1^2 (P_2^2 + m_{\text{UV}}^2)^3} \right\}. \tag{C4}$$

The remaining counterterms in the first row of Eq. (C2) are computed analogously. For the second and third rows, the K -operation acts on vacuum-type graphs with a dod of four. In these cases, we simply set $\mu = 0$ without performing any expansions.

With the sunset diagram now rendered locally finite through the R -operation, we proceed to the analytical integration of the energy integrals using the dLTD formula in Eq. (18). The form of the counterterms (see Eq. (C4)) is compatible with the starting point of dLTD in Eq. (14), allowing us to input Eq. (C2) directly into our algorithm that computes the energy integrals. The

higher-order residues introduced by degenerate propagators appearing in the counterterms are accessed by taking derivatives with respect to the on-shell energies of these propagators. Next, we provide an example computation of the energy integrals in the first term on the right-hand side of Eq. (C2), which corresponds to the bare sunset diagram.

Comparing Eq. (C1) and Eq. (14), we obtain $l = 2$, $n = 3$, $\mathbf{S}_1 = (1, 0, 1)$, $\mathbf{S}_2 = (0, 1, -1)$, $\boldsymbol{\varphi} = (1, 1, 0)$, and $\mathbf{E} = (|\vec{p}_1|, |\vec{p}_2|, |\vec{p}_1 - \vec{p}_2|)$. To perform the τ -integrals in Eq. (18), corresponding to Laplace transforms of nonsimplicial convex cones, we use the diagrammatic algorithm

introduced in Ref. [50]. Specifically, the sum over σ is interpreted as a sum over directed graphs, where only the acyclic ones contribute. For each of these acyclic graphs, a series of edge-contraction operations is performed, ultimately yielding a closed-form expression for the corresponding Laplace transform. For instance, one of the nonvanishing terms in the current example, with $\rho = (1, -1, 1)$ and $\sigma = (1, -1, -1)$, gives

$$\int_{\mathbb{R}_+^3} d\tau_1 d\tau_2 d\tau_3 e^{-\tau_1 E_1 + \tau_2 E_2 - \tau_3 E_3} \delta(\tau_1 - \tau_3) \delta(-\tau_2 + \tau_3) = \frac{1}{E_1 - E_2 + E_3}. \quad (\text{C5})$$

$$\begin{aligned} \text{Mercedes} &= 2g_s^2 N_f (N_c^2 - 1) \int \frac{d^3 \vec{p}_1}{(2\pi)^3} \frac{d^3 \vec{p}_2}{(2\pi)^3} \left\{ \frac{(E_1 E_2 + \vec{p}_1 \cdot \vec{p}_2) \Theta(E_1 - \mu)}{2E_1 2E_2 2E_3 (E_1 + E_2 + E_3)} - \frac{(-E_1 E_2 + \vec{p}_1 \cdot \vec{p}_2) \Theta(E_1 - \mu) \Theta(-E_2 + \mu)}{2E_1 2E_2 2E_3 (E_1 - E_2 + E_3)} \right. \\ &\quad \left. + \frac{(E_1 E_2 + \vec{p}_1 \cdot \vec{p}_2) \Theta(E_2 - \mu)}{2E_1 2E_2 2E_3 (E_1 + E_2 + E_3)} - \frac{(-E_1 E_2 + \vec{p}_1 \cdot \vec{p}_2) \Theta(-E_1 + \mu) \Theta(E_2 - \mu)}{2E_1 2E_2 2E_3 (-E_1 + E_2 + E_3)} \right\}, \end{aligned} \quad (\text{C6})$$

where only four distinct terms contribute. Note that most of the 2^{2n} ($n = 3$) terms vanish because they correspond to cyclic graphs or include a vanishing step function. By applying the same procedure to the seven counterterms to perform the energy integrals, we are now ready to proceed to the numerical evaluation of the spatial integrals in Eq. (C2).

The remaining three-dimensional spatial integrals in the UV-subtracted sunset diagram contain integrable singularities that hinder numerical integration. These singularities are flattened using the multichanneling procedure described in Appendix A. For the sunset diagram, there are three channels in total, specified by the loop momentum bases $\mathcal{B} = \{\{1, 2\}, \{1, 3\}, \{2, 3\}\}$. Each channel is then integrated separately using VEGAS5.6. With roughly 10^8 samples in total, the sum of the results for the three channels is

$$R \left(\text{Sunset} \right) = -0.00128338(23) \cdot \mu^4, \quad (\text{C7})$$

where $g_s = N_f = 1$, $N_c = 3$, and $m_{\text{UV}} = \mu$. The counterterms in Eq. (C2) are proportional to scaleless integrals, which evaluate to zero in dimensional regularization. Therefore, within dimensional regularization, the UV-subtracted sunset in Eq. (C7) is equal to the bare one that we are interested in. Comparing the final result in Eq. (C7) to the known value [59] shows an agreement within a relative error of 0.02%.

In Table I, we also present the result for the UV-subtracted three-loop QCD (Mercedes) diagram. The algorithmic steps in the dLTD evaluation of this dia-

gram follow those used in the two-loop sunset case discussed above. Compared to the two-loop case, the UV-subtracted Mercedes contains 21 counterterms, the bare diagram consists of 72 terms after performing the zero-component integrals (cf. Eq. (C6)), and the multichannel procedure involves 16 channels. With roughly 10^9 Monte-Carlo samples we obtain the following result for the UV-subtracted Mercedes:

$$R \left(\text{Mercedes} \right) = -1.4239(9) \cdot 10^{-4} \cdot \mu^4, \quad (\text{C8})$$

where $g_s = N_f = 1$, $N_c = 3$, and $m_{\text{UV}} = \mu$. Unlike in the two-loop case, the counterterms do not vanish in dimensional regularization for the Mercedes. Analytically computing these counterterms, which correspond to massive single-scale integrals, and adding them back to Eq. (C8) results in

$$\begin{aligned} \text{Mercedes} &= \left(-7.3136 \cdot 10^{-5} \cdot \frac{1}{\varepsilon} \right. \\ &\quad \left. - 0.00025654(9) + O(\varepsilon) \right) \cdot \mu^4, \end{aligned} \quad (\text{C9})$$

where we have set $\bar{\Lambda} = \mu$. This result agrees with the known value [59] within a relative error of 0.03%.

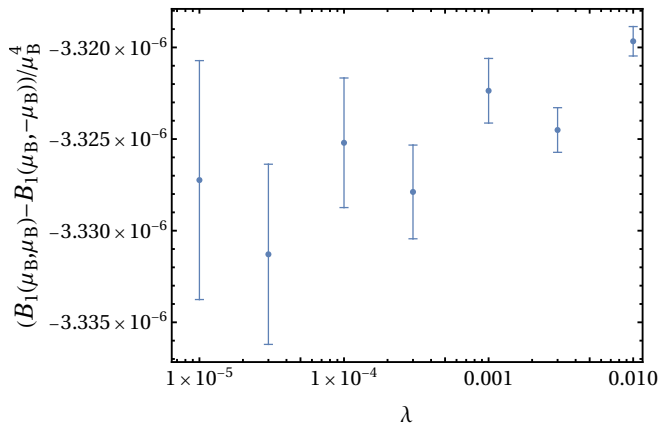


FIG. 2. Results for the numerical integration of Eq. (13) using seven different values for the fictitious gluon mass parameter $m_g = \lambda\mu_B$.

Appendix D: Regularization of non-local IR singularities in Eq. (13)

The cancellation of IR divergences in Eq. (13) is non-local, necessitating a regularization procedure for numerical evaluation. To address this, we introduce a small but nonzero mass in the gluonic on-shell energies as an IR regulator. Since the combination of Bugblatter diagrams we compute is IR safe after integration, the effect of the IR regulator should be insignificant, provided its numerical value is much smaller than the dominant scale of the integral, namely the baryon chemical potential μ_B . We verify the insensitivity by evaluating the integral with several different small values of the gluon mass m_g . Specifically, we define $m_g = \lambda\mu_B$ and compute the integral in Eq. (13) using seven values of λ within the range $[10^{-5}, 10^{-2}]$. The results are shown in Fig. 2. In the figure, we observe that all results are approximately equal within the error bars, except for the one with the largest IR regulator, $\lambda = 10^{-2}$. Therefore, as long as the fictitious gluon mass remains well below one percent of μ_B , the result is unaffected. However, for IR regulator values with λ less than 10^{-5} , the convergence rate of the numerical Monte Carlo integration significantly slows down. For the final result reported in the main text, we choose $\lambda = 10^{-5}$ as the most conservative option.

-
- [1] W. Busza, K. Rajagopal, and W. van der Schee, Heavy Ion Collisions: The Big Picture, and the Big Questions, *Ann. Rev. Nucl. Part. Sci.* **68**, 339 (2018), [arXiv:1802.04801 \[hep-ph\]](#).
- [2] J. N. Guenther, Overview of the QCD phase diagram: Recent progress from the lattice, *Eur. Phys. J. A* **57**, 136 (2021), [arXiv:2010.15503 \[hep-lat\]](#).
- [3] C. Ratti, Lattice QCD and heavy ion collisions: a review of recent progress, *Rept. Prog. Phys.* **81**, 084301 (2018), [arXiv:1804.07810 \[hep-lat\]](#).
- [4] G. Baym, T. Hatsuda, T. Kojo, P. D. Powell, Y. Song, and T. Takatsuka, From hadrons to quarks in neutron stars: a review, *Rept. Prog. Phys.* **81**, 056902 (2018), [arXiv:1707.04966 \[astro-ph.HE\]](#).
- [5] E. Annala, T. Gorda, A. Kurkela, J. Nättilä, and A. Vuorinen, Evidence for quark-matter cores in massive neutron stars, *Nature Phys.* **16**, 907 (2020), [arXiv:1903.09121 \[astro-ph.HE\]](#).
- [6] E. Annala, T. Gorda, J. Hirvonen, O. Komoltsev, A. Kurkela, J. Nättilä, and A. Vuorinen, Strongly interacting matter exhibits deconfined behavior in massive neutron stars, *Nature Commun.* **14**, 8451 (2023), [arXiv:2303.11356 \[astro-ph.HE\]](#).
- [7] P. Hasenfratz and F. Karsch, Chemical Potential on the Lattice, *Phys. Lett. B* **125**, 308 (1983).
- [8] F. Karsch and H. W. Wyld, Complex Langevin Simulation of the SU(3) Spin Model With Nonzero Chemical Potential, *Phys. Rev. Lett.* **55**, 2242 (1985).
- [9] I. Barbour, N.-E. Behilil, E. Dagotto, F. Karsch, A. Moreo, M. Stone, and H. W. Wyld, Problems with Finite Density Simulations of Lattice QCD, *Nucl. Phys. B* **275**, 296 (1986).
- [10] P. de Forcrand, Simulating QCD at finite density, *PoS LAT2009*, 010 (2009), [arXiv:1005.0539 \[hep-lat\]](#).
- [11] K. Nagata, Finite-density lattice QCD and sign problem: Current status and open problems, *Prog. Part. Nucl. Phys.* **127**, 103991 (2022), [arXiv:2108.12423 \[hep-lat\]](#).
- [12] B. B. Brandt, F. Cuteri, and G. Endrodi, Equation of state and speed of sound of isospin-asymmetric QCD on the lattice, *JHEP* **07**, 055, [arXiv:2212.14016 \[hep-lat\]](#).
- [13] R. Abbott, W. Detmold, M. Illa, A. Parreño, R. J. Perry, F. Romero-López, P. E. Shanahan, and M. L. Wagman, QCD constraints on isospin-dense matter and the nuclear equation of state, (2024), [arXiv:2406.09273 \[hep-lat\]](#).
- [14] I. Tews, T. Krüger, K. Hebeler, and A. Schwenk, Neutron matter at next-to-next-to-next-to-leading order in chiral effective field theory, *Phys. Rev. Lett.* **110**, 032504 (2013), [arXiv:1206.0025 \[nucl-th\]](#).
- [15] J. E. Lynn, I. Tews, J. Carlson, S. Gandolfi, A. Gezerlis, K. E. Schmidt, and A. Schwenk, Chiral Three-Nucleon Interactions in Light Nuclei, Neutron- α Scattering, and Neutron Matter, *Phys. Rev. Lett.* **116**, 062501 (2016), [arXiv:1509.03470 \[nucl-th\]](#).
- [16] C. Drischler, K. Hebeler, and A. Schwenk, Chiral interactions up to next-to-next-to-next-to-leading order and nuclear saturation, *Phys. Rev. Lett.* **122**, 042501 (2019), [arXiv:1710.08220 \[nucl-th\]](#).
- [17] C. Drischler, R. J. Furnstahl, J. A. Melendez, and D. R. Phillips, How Well Do We Know the Neutron-Matter Equation of State at the Densities Inside Neutron Stars? A Bayesian Approach with Correlated Uncertainties, *Phys. Rev. Lett.* **125**, 202702 (2020), [arXiv:2004.07232](#)

- [18] A. Kurkela, P. Romatschke, and A. Vuorinen, Cold Quark Matter, *Phys. Rev. D* **81**, 105021 (2010), [arXiv:0912.1856 \[hep-ph\]](#).
- [19] A. Kurkela and A. Vuorinen, Cool quark matter, *Phys. Rev. Lett.* **117**, 042501 (2016), [arXiv:1603.00750 \[hep-ph\]](#).
- [20] T. Gorda, A. Kurkela, P. Romatschke, S. Säppi, and A. Vuorinen, Next-to-Next-to-Next-to-Leading Order Pressure of Cold Quark Matter: Leading Logarithm, *Phys. Rev. Lett.* **121**, 202701 (2018), [arXiv:1807.04120 \[hep-ph\]](#).
- [21] T. Gorda, A. Kurkela, R. Paatelainen, S. Säppi, and A. Vuorinen, Soft Interactions in Cold Quark Matter, *Phys. Rev. Lett.* **127**, 162003 (2021), [arXiv:2103.05658 \[hep-ph\]](#).
- [22] T. Gorda, A. Kurkela, R. Paatelainen, S. Säppi, and A. Vuorinen, Cold quark matter at N3LO: Soft contributions, *Phys. Rev. D* **104**, 074015 (2021), [arXiv:2103.07427 \[hep-ph\]](#).
- [23] T. Gorda and S. Säppi, Cool quark matter with perturbative quark masses, *Phys. Rev. D* **105**, 114005 (2022), [arXiv:2112.11472 \[hep-ph\]](#).
- [24] T. Gorda, R. Paatelainen, S. Säppi, and K. Seppänen, Equation of State of Cold Quark Matter to $O(\alpha_s^3 \ln \alpha_s)$, *Phys. Rev. Lett.* **131**, 181902 (2023), [arXiv:2307.08734 \[hep-ph\]](#).
- [25] A. Kurkela, E. S. Fraga, J. Schaffner-Bielich, and A. Vuorinen, Constraining neutron star matter with Quantum Chromodynamics, *Astrophys. J.* **789**, 127 (2014), [arXiv:1402.6618 \[astro-ph.HE\]](#).
- [26] E. Annala, T. Gorda, A. Kurkela, and A. Vuorinen, Gravitational-wave constraints on the neutron-star-matter Equation of State, *Phys. Rev. Lett.* **120**, 172703 (2018), [arXiv:1711.02644 \[astro-ph.HE\]](#).
- [27] O. Komoltsev and A. Kurkela, How Perturbative QCD Constrains the Equation of State at Neutron-Star Densities, *Phys. Rev. Lett.* **128**, 202701 (2022), [arXiv:2111.05350 \[nucl-th\]](#).
- [28] R. Somasundaram, I. Tews, and J. Margueron, Perturbative QCD and the neutron star equation of state, *Phys. Rev. C* **107**, L052801 (2023), [arXiv:2204.14039 \[nucl-th\]](#).
- [29] O. Komoltsev, R. Somasundaram, T. Gorda, A. Kurkela, J. Margueron, and I. Tews, Equation of state at neutron-star densities and beyond from perturbative QCD, (2023), [arXiv:2312.14127 \[nucl-th\]](#).
- [30] T. Gorda, O. Komoltsev, A. Kurkela, and A. Mazeliauskas, Bayesian uncertainty quantification of perturbative QCD input to the neutron-star equation of state, *JHEP* **06**, 002, [arXiv:2303.02175 \[hep-ph\]](#).
- [31] B. P. Abbott *et al.* (LIGO Scientific, Virgo), GW170817: Observation of Gravitational Waves from a Binary Neutron Star Inspiral, *Phys. Rev. Lett.* **119**, 161101 (2017), [arXiv:1710.05832 \[gr-qc\]](#).
- [32] B. P. Abbott *et al.* (LIGO Scientific, Virgo), GW170817: Measurements of neutron star radii and equation of state, *Phys. Rev. Lett.* **121**, 161101 (2018), [arXiv:1805.11581 \[gr-qc\]](#).
- [33] B. P. Abbott *et al.* (LIGO Scientific, Virgo), Properties of the binary neutron star merger GW170817, *Phys. Rev. X* **9**, 011001 (2019), [arXiv:1805.11579 \[gr-qc\]](#).
- [34] H. T. Cromartie *et al.* (NANOGrav), Relativistic Shapiro delay measurements of an extremely massive millisecond pulsar, *Nature Astron.* **4**, 72 (2019), [arXiv:1904.06759 \[astro-ph.HE\]](#).
- [35] J. Nättilä, M. C. Miller, A. W. Steiner, J. J. E. Kajava, V. F. Suleimanov, and J. Poutanen, Neutron star mass and radius measurements from atmospheric model fits to X-ray burst cooling tail spectra, *Astron. Astrophys.* **608**, A31 (2017), [arXiv:1709.09120 \[astro-ph.HE\]](#).
- [36] M. C. Miller *et al.*, PSR J0030+0451 Mass and Radius from *NICER* Data and Implications for the Properties of Neutron Star Matter, *Astrophys. J. Lett.* **887**, L24 (2019), [arXiv:1912.05705 \[astro-ph.HE\]](#).
- [37] J. B. Kogut and D. K. Sinclair, Lattice QCD at finite temperature and density in the phase-quenched approximation, *Phys. Rev. D* **77**, 114503 (2008), [arXiv:0712.2625 \[hep-lat\]](#).
- [38] C. Vafa and E. Witten, Parity Conservation in QCD, *Phys. Rev. Lett.* **53**, 535 (1984).
- [39] T. D. Cohen, QCD inequalities for the nucleon mass and the free energy of baryonic matter, *Phys. Rev. Lett.* **91**, 032002 (2003), [arXiv:hep-ph/0304024](#).
- [40] Y. Fujimoto and S. Reddy, Bounds on the equation of state from QCD inequalities and lattice QCD, *Phys. Rev. D* **109**, 014020 (2024), [arXiv:2310.09427 \[nucl-th\]](#).
- [41] D. Lee, Pressure inequalities for nuclear and neutron matter, *Phys. Rev. C* **71**, 044001 (2005), [arXiv:nucl-th/0407101](#).
- [42] G. D. Moore and T. Gorda, Bounding the QCD Equation of State with the Lattice, *JHEP* **12**, 133, [arXiv:2309.15149 \[nucl-th\]](#).
- [43] D. T. Son, Superconductivity by long range color magnetic interaction in high density quark matter, *Phys. Rev. D* **59**, 094019 (1999), [arXiv:hep-ph/9812287](#).
- [44] H. Malekzadeh and D. H. Rischke, Gluon self-energy in the color-flavor-locked phase, *Phys. Rev. D* **73**, 114006 (2006), [arXiv:hep-ph/0602082](#).
- [45] M. G. Alford, A. Schmitt, K. Rajagopal, and T. Schäfer, Color superconductivity in dense quark matter, *Rev. Mod. Phys.* **80**, 1455 (2008), [arXiv:0709.4635 \[hep-ph\]](#).
- [46] Y. Fujimoto, Enhanced contribution of the pairing gap to the QCD equation of state at large isospin chemical potential, *Phys. Rev. D* **109**, 054035 (2024), [arXiv:2312.11443 \[hep-ph\]](#).
- [47] S. Catani, T. Gleisberg, F. Krauss, G. Rodrigo, and J.-C. Winter, From loops to trees by-passing Feynman's theorem, *JHEP* **09**, 065, [arXiv:0804.3170 \[hep-ph\]](#).
- [48] Z. Capatti, V. Hirschi, D. Kermanschah, and B. Ruijl, Loop-Tree Duality for Multiloop Numerical Integration, *Phys. Rev. Lett.* **123**, 151602 (2019), [arXiv:1906.06138 \[hep-ph\]](#).
- [49] Z. Capatti, V. Hirschi, D. Kermanschah, A. Pelloni, and B. Ruijl, Numerical Loop-Tree Duality: contour deformation and subtraction, *JHEP* **04**, 096, [arXiv:1912.09291 \[hep-ph\]](#).
- [50] Z. Capatti, Exposing the threshold structure of loop integrals, *Phys. Rev. D* **107**, L051902 (2023), [arXiv:2211.09653 \[hep-th\]](#).
- [51] S. Weinzierl, *Feynman Integrals* (Springer Cham, 2022).
- [52] J. P. Blaizot, E. Iancu, and A. Rebhan, Quark number susceptibilities from HTL resummed thermodynamics, *Phys. Lett. B* **523**, 143 (2001), [arXiv:hep-ph/0110369](#).
- [53] P. Navarrete and Y. Schröder, Tackling the infamous g^6 term of the QCD pressure, *PoS* **LL2022**, 014 (2022), [arXiv:2207.10151 \[hep-ph\]](#).
- [54] P. Navarrete and Y. Schröder, unpublished.

- [55] A. Kärkkäinen, P. Navarrete, M. Nurmela, R. Paatelainen, and A. Vuorinen, unpublished.
- [56] K. G. Chetyrkin and F. V. Tkachov, Integration by parts: The algorithm to calculate β -functions in 4 loops, *Nucl. Phys. B* **192**, 159 (1981).
- [57] S. Laporta, High-precision calculation of multiloop Feynman integrals by difference equations, *Int. J. Mod. Phys. A* **15**, 5087 (2000), [arXiv:hep-ph/0102033](https://arxiv.org/abs/hep-ph/0102033).
- [58] J. M. Henn, Multiloop integrals in dimensional regularization made simple, *Phys. Rev. Lett.* **110**, 251601 (2013), [arXiv:1304.1806](https://arxiv.org/abs/1304.1806) [hep-th].
- [59] A. Vuorinen, The Pressure of QCD at finite temperatures and chemical potentials, *Phys. Rev. D* **68**, 054017 (2003), [arXiv:hep-ph/0305183](https://arxiv.org/abs/hep-ph/0305183).
- [60] Y. Schroder, A fresh look on three-loop sum-integrals, *JHEP* **08**, 095, [arXiv:1207.5666](https://arxiv.org/abs/1207.5666) [hep-ph].
- [61] A. Gynther, M. Laine, Y. Schroder, C. Torrero, and A. Vuorinen, Four-loop pressure of massless $O(N)$ scalar field theory, *JHEP* **04**, 094, [arXiv:hep-ph/0703307](https://arxiv.org/abs/hep-ph/0703307).
- [62] A. Gynther, A. Kurkela, and A. Vuorinen, The $N(f)^{*3}g^{*6}$ term in the pressure of hot QCD, *Phys. Rev. D* **80**, 096002 (2009), [arXiv:0909.3521](https://arxiv.org/abs/0909.3521) [hep-ph].
- [63] T. Gorda, A. Kurkela, J. Österman, R. Paatelainen, S. Säppi, P. Schicho, K. Seppänen, and A. Vuorinen, Degenerate fermionic matter at N3LO: Quantum electrodynamics, *Phys. Rev. D* **107**, L031501 (2023), [arXiv:2204.11893](https://arxiv.org/abs/2204.11893) [hep-ph].
- [64] I. Ghisoiu, T. Gorda, A. Kurkela, P. Romatschke, S. Säppi, and A. Vuorinen, On high-order perturbative calculations at finite density, *Nucl. Phys. B* **915**, 102 (2017), [arXiv:1609.04339](https://arxiv.org/abs/1609.04339) [hep-ph].
- [65] J. Österman, P. Schicho, and A. Vuorinen, Integrating by parts at finite density, *JHEP* **08**, 212, [arXiv:2304.05427](https://arxiv.org/abs/2304.05427) [hep-ph].
- [66] S. Laporta, High precision epsilon expansions of massive four loop vacuum bubbles, *Phys. Lett. B* **549**, 115 (2002), [arXiv:hep-ph/0210336](https://arxiv.org/abs/hep-ph/0210336).
- [67] <https://github.com/gplepage/vegas>.
- [68] J. A. M. Vermaseren, Axodraw, *Comput. Phys. Commun.* **83**, 45 (1994).
- [69] N. N. Bogoliubov and O. S. Parasiuk, On the Multiplication of the causal function in the quantum theory of fields, *Acta Math.* **97**, 227 (1957).
- [70] K. Hepp, Proof of the Bogolyubov-Parasiuk theorem on renormalization, *Commun. Math. Phys.* **2**, 301 (1966).
- [71] W. Zimmermann, Convergence of Bogolyubov's method of renormalization in momentum space, *Commun. Math. Phys.* **15**, 208 (1969).
- [72] Z. Capatti, V. Hirschi, and B. Ruijl, Local unitarity: cutting raised propagators and localising renormalisation, *JHEP* **10**, 120, [arXiv:2203.11038](https://arxiv.org/abs/2203.11038) [hep-ph].